PAPER

Study of the rainbow-like pattern in the elastic scattering of ^{16}O on ^{27}Al at $E_{lab.}$ = 100 MeV

J. Phys. G: Nucl. Part. Phys. **40** (2013) 105101 (12pp) doi:10.1088/0954-3899/40/10/105101

Study of the rainbow-like pattern in the elastic scattering of ^{16}O on ^{27}Al at $E_{\text{lab.}} = 100$ MeV

J R B Oliveira[1], F Cappuzzello[2,3], L C Chamon[1], D Pereira[1,6], C Agodi[3], M Bondi[2,3], D Carbone[2,3], M Cavallaro[3], A Cunsolo[3], M De Napoli[4], A Foti[2,4], L R Gasques[1], P R S Gomes[5], R Linares[5], J Lubian[5], D Nicolosi[2,3] and S Tropea[2,3]

[1] Departamento de Física Nuclear, Instituto de Física da Universidade de São Paulo, Caixa Postal 66318, São Paulo, SP, 05315-970, Brazil
[2] Dipartimento di Fisica e Astronomia Universita di Catania, I-95125, Catania, Italy
[3] INFN, Laboratori Nazionali del Sud, I-95125, Catania, Italy
[4] INFN-Sez. Catania, via S. Sofia, 64, I-95125, Catania, Italy
[5] Instituto de Física da Universidade Federal Fluminense, Av. Litoranea s/n, Niterói, RJ, 24210-340, Brazil

E-mail: Jose.Oliveira@if.usp.br and zero@if.usp.br

Received 23 April 2013
Published 22 August 2013
Online at stacks.iop.org/JPhysG/40/105101

Abstract
Recently, a rainbow pattern in the elastic scattering of ^{16}O + ^{27}Al at $E_{\text{lab.}} = 100$ MeV was reported. In the present paper, we show that the predicted change of slope of the cross section, as a function of angle, is mostly due to the far-side component of the scattering, which is affected by the inelastic couplings. The experimental data is consistent with the calculations up to the inflection point, where the effect of the couplings is significant. New experimental data, in very good agreement with the theoretical expectations around the Coulomb rainbow angle, are also presented.

(Some figures may appear in colour only in the online journal)

1. Introduction

Optical phenomena such as diffraction, rainbows, etc., also occur in the context of heavy-ion nuclear reactions [1–6]. Indeed, within the optical model (OM), widely employed in elastic scattering data analyses, the nuclear collision is described making use of a complex optical potential, with clear analogy to the problem of the scattering of light by a refractive and absorptive optical medium, with a complex refractive index. From a classical point of view, the rainbow phenomenon is an accumulation of trajectories (of the collision partners) near

[6] Deceased.

a limiting angle (or caustic), resulting in an infinite differential cross section at that angle. This behaviour can be understood through the corresponding deflection function, since the classical cross section is inversely proportional to its derivative. In the quantum mechanics formalism, where trajectories are not well defined, the deflection function can be obtained from the derivative of the phase-shifts and used to interpret these phenomena. However, in relatively heavy systems, OM analyses have shown that the deflection function monotonically decreases as a function of the angular momentum due to the strong reflection from the surface, generated by the imaginary part of the optical potential [9, 10]. Here, we show that the coupling of elastic with inelastic channels can generate the dynamical conditions for the nuclear rainbow to emerge in such systems. Additional information on the study of the rainbow features can be extracted from the decomposition of the elastic amplitude into the near-side and far-side components within the approach of Fuller [7, 8]. The far-side or refractive component has been shown to have an important role in the resolution of potential ambiguities [4, 5].

The elastic scattering of ^{16}O on ^{27}Al at $E_{\rm lab.} = 100$ MeV has recently been measured in a high precision experiment [11]. The data were shown to be consistent with the theoretical calculations which predict a rainbow-like scattering in this system as a consequence of the couplings to the inelastic target excitations [12]. In the present paper, we investigate this phenomenon in more detail, through analysis of the classical and quantum deflection functions considering absorption (through the presence of an imaginary part of the optical potential), together with the study of the near-side and far-side contributions.

The São Paulo potential (SPP) [13] has been used in all calculations in the present work. The SPP is a theoretical model for the heavy-ion nuclear interaction. The energy dependence of this interaction is derived from the effects of the Pauli non-locality. The model has been successfully applied in data analyses for different reaction channels and over a wide energy region. In many works, it is used in OM elastic scattering data analyses with an optical potential given by: $U_{\rm Opt}(R) = (N_R + {\rm i}N_I)\, V_{\rm SPP}(R)$, where N_R and N_I are normalization factors for the real and imaginary parts of the potential, respectively. In several cases the data are well described with $N_R = 1$ and $N_I = 0.78$, as found in [14]. We name the use of such N_R and N_I values as a standard SPP within the context of the OM.

The paper is organized as follows. Section 2 presents a comparison between theoretical and experimental angular distributions for ^{16}O + ^{27}Al at $E_{\rm lab.} = 100$ MeV. Sections 3 and 4 present the classical and the quantum approaches, respectively. The corresponding results for the deflection functions are shown in section 5. The near–far decomposition for this system is discussed in section 6. The final remarks are presented in section 7.

2. Comparison between theoretical and experimental angular distributions

The SPP was assumed in the coupled-channel (CC) calculations (with CC code FRESCO [15]) of the elastic scattering for ^{16}O on ^{27}Al at $E_{\rm lab.} = 100$ MeV (see [12] for details). In these calculations the elastic channel has been coupled to the low-lying states of ^{27}Al using the weak coupling model of the $I^\pi = \frac{5}{2}^+$ proton hole in the ^{28}Si core with the collective 2^+ excitation of ^{28}Si, as explained in [12, 16]. A total of 550 partial waves were considered in the calculations. The SPP was adopted as the optical potential with $N_R = 1$ and $N_I = 0.6$. This lower N_I value (relative to the standard one) not only accounts for reduced losses of flux from the larger model space in CC calculations compared to OM, but is also justified in a more general theoretical and experimental perspective, including this and other nuclear systems [16]. We regard these calculations as the most reliable ones currently available. The results are shown in figure 1 by the (black) solid line. The pure OM (dash–dot–dot line) calculations (with $N_I = 0.6$) is also shown for comparison. As an effect of the couplings, there is a redistribution of the flux from

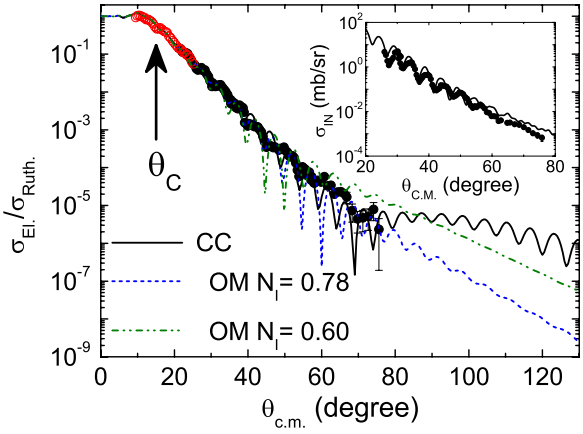

Figure 1. Elastic and inelastic scattering for $^{16}O + ^{27}Al$ at $E_{LAB} = 100$ MeV. The closed symbols are the experimental data from [12], while the (red) open symbols are the new data reported for the first time in the present paper. The lines in the figure correspond to the results of the optical model (OM) calculations with two different imaginary potential normalization parameter values: $N_I = 0.60$ (dash–dot–dotted) and the *standard* $N_I = 0.78$ (dashed). The CC calculation with $N_I = 0.60$, as specified in [12, 16], is represented by the solid line. The arrow indicates the position of the Coulomb rainbow angle. The convolution of the experimental resolution was not included in the theoretical curves, but has a negligible effect except for the reduction of the depths of the sharp minima around 70°. The inset shows the inelastic scattering data points (sum of the first low-lying inelastic states [12]), and the corresponding CC results (solid line).

the $60^\circ < \theta < 80^\circ$ region to that above $\theta = 90^\circ$. We point out that the couplings to inelastic channels are not usually considered in data analysis at relatively high energies. However, we observe that they can be very important, as in the present case (∼6 MeV/nucleon) and in others [16]. Figure 1 also presents the standard OM ($N_I = 0.78$) predictions for the elastic angular distribution (dash line). The closed (black) symbols correspond to the elastic scattering cross section data presented in [12], while the open (red) ones are new data reported here for the first time. These data result from complementary analysis of the same experiment reported in [11, 12]. They are consistent with the predictions in the Coulomb rainbow region, with the maximum at ∼10°. Without any free parameters, both (standard OM and CC) calculations reasonably well describe the trend of the elastic scattering data, up to the highest angle measured. However, there is an inflection around 70° and, for $\theta > 80^\circ$, the CC results for the differential cross sections become orders of magnitude larger than those from the standard OM. The CC elastic cross section remains in the same landing, $10^{-5} \leqslant \sigma_{El.}/\sigma_{\mathrm{Ruth.}} \leqslant 10^{-6}$, over a wide angular region, from 60° to about 120°, where both OM calculations present an exponentially decreasing behaviour. It is this contrasting pattern of the CC calculations relative to the OM ones which we associate with the rainbow.

As already commented, both CC and standard OM calculations describe the elastic scattering data set (up to 75°) present in figure 1, and one might question the reliability of the rainbow pattern prediction. First of all, the CC formalism is, of course, more fundamental than the standard OM approach. In addition, the CC calculations consistently provide a good description of the experimental *inelastic* cross sections (see the inset of figure 1). Furthermore, the CC results are also in good agreement with the experimental data of other processes (such as transfer, fusion, and deep inelastic collisions) which have been measured for this system at other energies [16]. Thus, enough experimental corroboration of these CC calculations

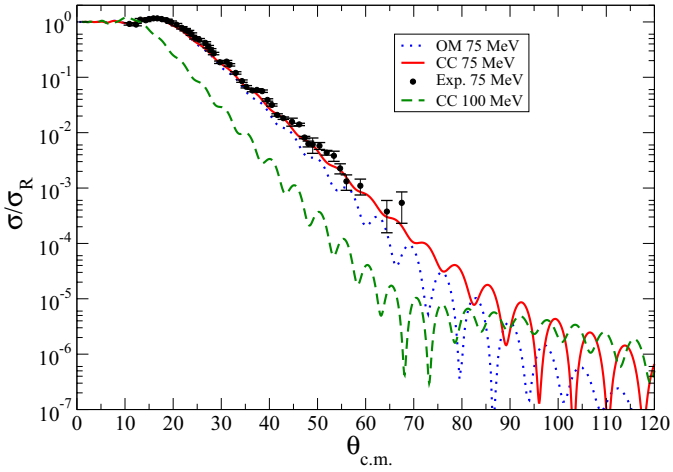

Figure 2. Elastic scattering angular distributions for ^{16}O + ^{28}Si at 75 MeV. Experimental data (closed circles—extracted from ref. [17]) compared to CC (2^+ state, red solid line) and OM (blue dotted line) results (both with $N_I = 0.60$). The CC results at 100 MeV (dashed) are also shown for comparison.

is available to support the present study and further justify experimental and theoretical investigations of channel coupling-related rainbow patterns.

In order to study the dependence on the beam energy of the rainbow pattern, we have also considered the data for the ^{16}O + ^{28}Si system at 75 MeV [17]. We present our CC calculations for this case, again with 550 partial waves, in figure 2. At this energy the rainbow pattern is predicted to be absent, and the exponential decay trend as a function of angle, predicted for the elastic scattering, proceeds at least up to $\theta \sim 100^\circ$. The CC theoretical cross section is consistent with the data where they are available. The coupling to the 2^+ excited state mildly affects the angular distribution in this case. We point out that a reasonable agreement with the inelastic data is also obtained [18]. The result obtained by changing only one parameter, the beam energy, to 100 MeV, is also presented. It shows a quite different pattern, which is, of course, very similar to the ^{27}Al result (figure 1). This indicates that a minimum energy around 100 MeV is necessary for the rainbow pattern formation in these systems.

The occurrence of a rainbow pattern in heavy-ion nuclear collisions has already been reported in many papers (for reviews, see [1–3, 5]). In the next sections we provide a brief review on the classical, semi-classical and quantum descriptions of a rainbow. Then, we return to considering how the present experimental data, although limited, can be considered to corroborate the CC calculations.

3. Classical trajectories

Figure 3(a) shows a schematic view of the classical trajectory of a particle scattered by a centre of force. The impact parameter b and deflection angle Θ are also represented in the figure. Classically, the deflection angle can be obtained from

$$\Theta = \pi - 2\int_{r_0}^{\infty} \frac{b/r^2}{\sqrt{1 - b^2/r^2 - V(r)/E_{c.m.}}}\,\mathrm{d}r, \tag{1}$$

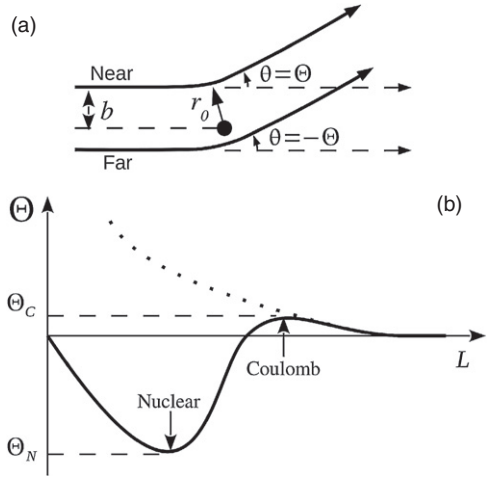

Figure 3. (a) The solid lines represent schematic classical trajectories of a particle around a centre of force (closed circle). One of the trajectories scatters on the near-side ($\Theta > 0$) and the other on the far-side ($\Theta < 0$) of the scattering centre, both resulting in the same scattering angle θ ($0 \leqslant \theta \leqslant \pi$). The impact parameter b and the turning point r_0 are shown for one of the trajectories. The classical deflection angle of the trajectories is $\Theta = \pm\theta - 2m\pi$, with integer $m \geqslant 0$. (b) The nuclear and Coulomb rainbows are indicated in the schematic deflection function (solid line). The dotted line represents a pure Coulomb deflection function.

where $V(r)$ and $E_{c.m.}$ represent the central potential and total energy, respectively. The r_0 parameter in this equation is the turning point (distance of closest approach) of the trajectory. The angular momentum L is related to the impact parameter through

$$L = \mu v_0 b, \tag{2}$$

where μ is the reduced mass of the system and v_0 is the asymptotic ($r \to \infty$) velocity.

Within the semi-classical approach, the angular momentum values are obtained from the Langer modification

$$L = (\ell + 1/2)\hbar. \tag{3}$$

For the scattering of two point-like particles interacting by a pure Coulomb potential $V(r) = Z_1 Z_2 e^2/r$, the classical and semi-classical deflection angles are given by

$$\Theta_C(b) = 2\arctan\left(\frac{Z_1 Z_2 e^2}{2E_{c.m.}b}\right) \tag{4}$$

and

$$\Theta_C(\ell) = 2\arctan\left(\frac{\eta}{\ell}\right), \tag{5}$$

respectively, where $\eta = Z_1 Z_2 e^2/\hbar v_0$ is the Sommerfeld parameter.

Classically, the cross section at a scattering angle θ, defined in the region $0 \leqslant \theta \leqslant \pi$, is given by

$$\frac{\mathrm{d}\sigma}{\mathrm{d}\Omega} = \frac{1}{\sin\theta}\sum\frac{b}{|\mathrm{d}\Theta/\mathrm{d}b|} = \frac{1}{2\mu E_{c.m.}\sin\theta}\sum\frac{L}{|\mathrm{d}\Theta/\mathrm{d}L|}, \tag{6}$$

where the sum is performed over all trajectories that scatter to the same θ value. If the deflection function has a relative maximum or minimum ($\mathrm{d}\Theta/\mathrm{d}L = 0$), the cross section has a singularity. The angle at which this occurs is known as the rainbow angle (see figure 3(b)).

Different trajectories can result in the same scattering angle, as illustrated in figure 3(a). For large impact parameters, the Coulomb interaction dominates and the corresponding trajectories result in $\Theta > 0$. These trajectories are considered to be of the near-side type (figure 3(a)). On the other hand, for small impact parameters, due to the strong nuclear interaction, $\Theta < 0$ is obtained (far-side trajectories). The Coulomb rainbow occurs in a region where the nuclear potential is small compared to the Coulomb one and is related to near-side trajectories, while the nuclear rainbow arises from the far-side ones (see figures 3(b) and (a)), when nuclear forces dominate.

4. Quantum approach

Within quantum mechanics, the amplitude for elastic scattering is given by

$$f(\theta) = f_C(\theta) - \frac{\mathrm{i}}{2k}\sum_{\ell}(2\ell+1)\,\mathrm{e}^{2\mathrm{i}\sigma_\ell}(S_\ell - 1)P_\ell(\cos\theta), \tag{7}$$

where f_C is the pure Coulomb amplitude, σ_ℓ are the Coulomb phase-shifts and S_ℓ is the elastic S-matrix. We write the S-matrix as

$$S_\ell = |S_\ell|\,\mathrm{e}^{2\mathrm{i}\delta_\ell}. \tag{8}$$

The deflection function is defined in the context of semi-classical mechanics by (see e.g. [19])

$$\Theta(\ell) = \Theta_C(\ell) + 2\frac{\mathrm{d}\delta_\ell}{\mathrm{d}\ell}. \tag{9}$$

However, the nuclear phase-shifts of equation (8) can be modified as $\delta_\ell \to \delta_\ell + n\pi$ (n integer) without affecting the S-matrix. This should be taken into account when obtaining the deflection function from the discrete version of equation (9), as discussed in the next section.

The elastic amplitude can be decomposed in the near-side and far-side components through

$$f_N(\theta) = f_{CN}(\theta) - \frac{\mathrm{i}}{2k}\sum_{\ell}(2\ell+1)\,\mathrm{e}^{2\mathrm{i}\sigma_\ell}(S_\ell - 1)\tilde{Q}_\ell^-(\cos\theta), \tag{10}$$

$$f_F(\theta) = f_{CF}(\theta) - \frac{\mathrm{i}}{2k}\sum_{\ell}(2\ell+1)\,\mathrm{e}^{2\mathrm{i}\sigma_\ell}(S_\ell - 1)\tilde{Q}_\ell^+(\cos\theta), \tag{11}$$

where f_{CN} and f_{CF} correspond to the near-side and far-side components of the Coulomb amplitude [8]. $\tilde{Q}_\ell^+$ and $\tilde{Q}_\ell^-$ are the opposite travelling wave components of the standing wave Legendre polynomial. The elastic cross section is formally obtained from $\frac{\mathrm{d}\sigma}{\mathrm{d}\Omega} = |f(\theta)|^2$ and, as usual, we define the near-side and far-side cross sections as: $\frac{\mathrm{d}\sigma_{N(F)}}{\mathrm{d}\Omega} = |f_{N(F)}(\theta)|^2$. In a practical calculation, the sum over ℓ is truncated at a maximum value (ℓ_{Max}, for which the nuclear interaction can be neglected) and a model interaction is required to determine S_ℓ. Alternatively the S_ℓ can be directly parametrized without relying on any assumption about the nuclear interaction [20].

5. Classical and quantum deflection functions

Figure 4 (top) presents the classical results of the deflection function for ^{16}O + ^{27}Al at $E_{\mathrm{lab.}} = 100$ MeV. The angular momentum is represented in this figure by the ℓ parameter of equation (3). In these calculations, the SPP was assumed for the nuclear interaction and the Coulomb potential was obtained from double-folding procedures. The classical trajectories for some ℓ values are shown in figure 4 (bottom). One can see an almost orbiting condition for $\ell = 35$ which results in nearly the same scattering angle θ of $\ell = 36$. Figure 5 presents the

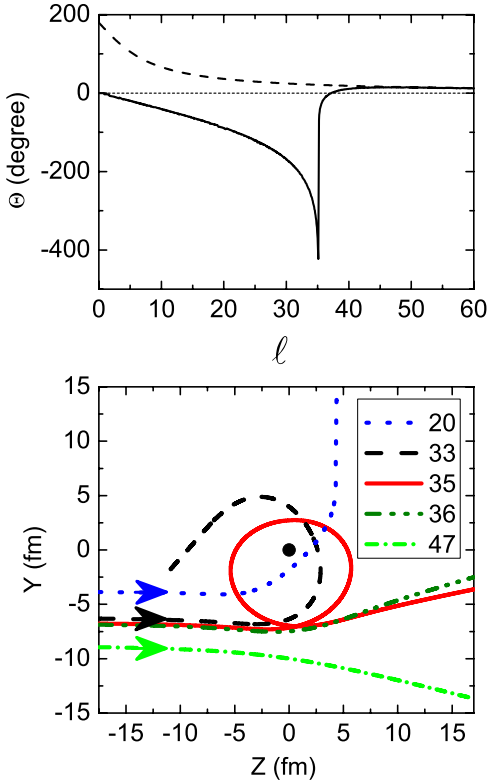

Figure 4. (Top) The solid curve represents the classical deflection function for the ^{16}O + ^{27}Al system at $E_{\mathrm{LAB}} = 100$ MeV, obtained assuming the SPP for the nuclear interaction and a folding procedure for the Coulomb potential. The dashed curve corresponds to the pure Coulomb deflection function. An unstable orbiting singularity appears between $\ell = 35$ and $\ell = 36$. (Bottom) Classical trajectories for some ℓ values as indicated in the figure. The closed circle represents the centre of force.

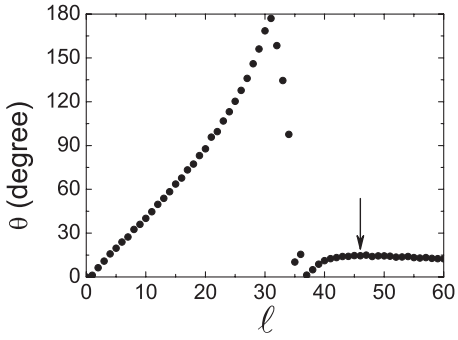

Figure 5. The classical scattering angle as a function of the ℓ parameter. The arrow indicates the position of the Coulomb rainbow.

corresponding scattering angle as a function of ℓ. No indication of the nuclear rainbow can be found in this figure, but it is possible to determine a Coulomb rainbow (the maximum of the deflection function) around $\ell = 47$ with $\theta_C \approx 15^\circ$, which clearly appears in the new data set (red open circles) presented in figure 1.

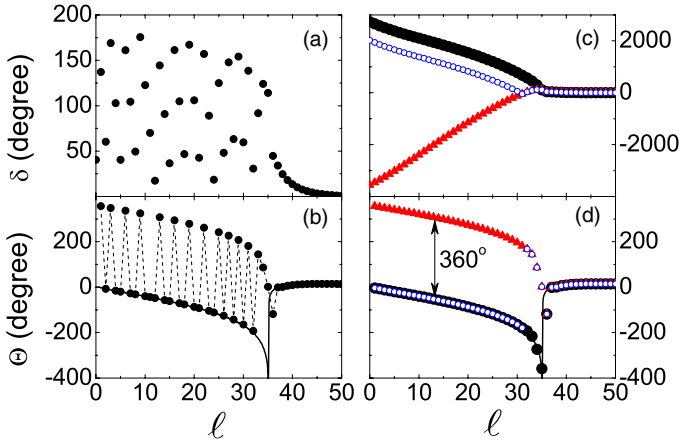

Figure 6. (a) and (c) Nuclear phase-shifts obtained from optical model calculations with vanishing imaginary potential. The phase-shifts in (a) correspond to values in the region $0 \leqslant \delta_\ell \leqslant 180^\circ$, while those in (c) were displaced by $n \times 180^\circ$ (n integer) relative to those in (a), with the symbols representing possible different sets of values of n, in order to obtain rather smooth behaviours. Note the change of scale in these figures. (b) The solid line corresponds to the classical deflection function, while the symbols, joined by straight dashed lines, represent Θ values obtained from equation (9) with the phase-shifts shown in (a). (d) Deflection functions, obtained with the corresponding sets of phase-shifts shown in (c), calculated from equations (9) and (12). The solid line again corresponds to the classical deflection function.

With the aim of comparing the classical deflection function with the corresponding quantum results, we performed OM calculations with a vanishing imaginary potential ($N_I = 0$). Figure 6(a) presents the resulting phase-shifts defined in the region of $0 \leqslant \delta_\ell \leqslant \pi$. Since we deal with a discrete ℓ variable, it is necessary to assume a procedure for calculating the derivative $\frac{\mathrm{d}\delta}{\mathrm{d}\ell}$ and consequently the deflection function from equation (9). The results shown in figure 6(b) were obtained with

$$\frac{\mathrm{d}\delta}{\mathrm{d}\ell}(\ell) \approx \delta_\ell - \delta_{\ell-1}. \tag{12}$$

The phase-shifts can be displaced by $n \times 180^\circ$ (n integer) without altering the S-matrix, resulting in an ambiguity in the determination of Θ from equation (9). The three possible phase-shift sets in figure 6(c) (represented by three different symbols) were rearranged by $n \times 180^\circ$ in relation to that of figure 6(a) in order to present a smooth behaviour (note the change of scale between figures 6(a) and (c)). The corresponding Θ values are shown in figure 6(d). The results of the closed-black-circle set are quite similar to the classical deflection function (solid line in figure 6(d)), as should be the case, since the OM calculations were performed with a vanishing imaginary potential. The other two sets present, for some ℓ values, differences of 360° relative to the Θ values of the closed-black-circle set. Therefore, the three sets result in the same scattering angle θ, which is the directly observable quantity. Thus, instead of Θ versus ℓ, from now on we prefer to present the scattering angle function, θ versus ℓ. Despite removing the above mentioned Θ ambiguity, this choice does not permit us to distinguish the fluxes coming from positive and negative deflection angles. Such a distinction can be made by the near–far decomposition, discussed in the next section. An alternative approach would be to plot the complex turning point branches as a function of the real scattering angle obtained from a semi-classical procedure with extension to complex trajectories and angular momenta

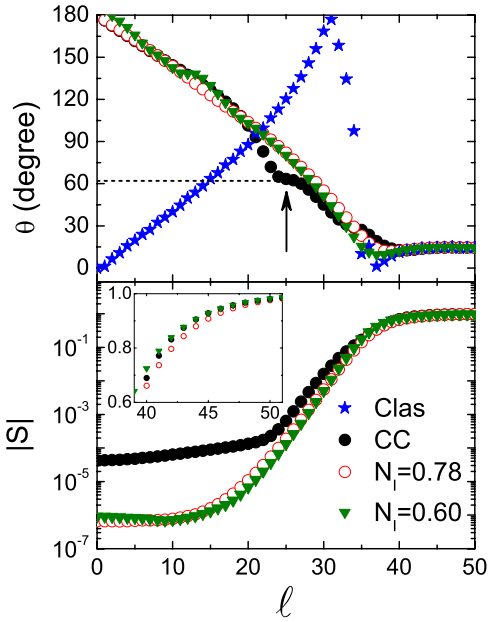

Figure 7. (Top) Scattering angle functions. (Bottom) Modulus of the *S*-matrix obtained from OM (standard: open circles; $N_I = 0.6$: closed triangles) and CC (closed circles) calculations. The result of the classical ($N_I = 0$) function (stars) is shown in the top figure. The inset presents the modulus of the *S*-matrix in a linear scale in the $40 \leqslant \ell \leqslant 50$ region.

(as in [5, 21]), which is a generalization of the deflection function appropriate for dealing with complex potentials. We plan to attempt this approach in the future.

Figure 7 (top) shows the scattering angle functions from the classical calculation (practically the same as the $N_I = 0$ result), together with the OM, for complex potential normalization factors of $N_I = 0.78$ and $N_I = 0.6$, and CC (with $N_I = 0.6$) results. The effect of the imaginary potential is strong since the classical and OM results are very different. The CC results are slightly different from the OM ones and might indicate a possible formation of a nuclear rainbow at $\ell \approx 25$ (arrow in the figure). However, the corresponding scattering angles are concentrated in a small interval around $\theta_R \approx 60^\circ$ (see figure 7 (top)), which is significantly smaller than the angular region of the broad bump of figure 1. Furthermore, the *S*-matrix reaches very small values for small angular momenta (see figure 6 (bottom)). Therefore, it is important to test whether the elastic scattering cross sections are sensitive to the phase-shifts for $\ell \approx 25$. We performed calculations to verify this point. We assumed the *S*-matrix from the CC calculation as a basis for calculating cross sections. Then, we obtained angular distributions with this *S*-matrix, but imposing $S_\ell = 0$ for $0 \leqslant \ell \leqslant \ell_{\rm CUT}$. Figure 8(a) shows angular distributions for different $\ell_{\rm CUT}$ values. Clearly, the cross sections are insensitive to the region $\ell \leqslant 25$, but a cut-off at $\ell = 30$ strongly affects the magnitude of the cross sections at backward angles. Therefore, the partial waves up to $\ell \approx 25$ in the CC scattering angle function of figure 6 (top) contribute negligibly to the rainbow structure in the angular distribution. In conclusion, the comparatively larger modulus of *S* of the CC calculations in the range from $\ell = 25$ to 35 (figure 7 (bottom)) is related to the possibility of observation of the rainbow pattern.

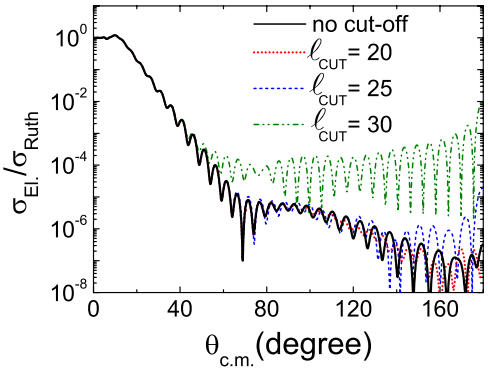

Figure 8. The solid line represents the elastic scattering angular distribution obtained from the CC calculations. The other lines correspond to calculations with the same S-matrix, but imposing $S_\ell = 0$ in the $0 \leqslant \ell \leqslant \ell_{\rm CUT}$ range for different $\ell_{\rm CUT}$ values.

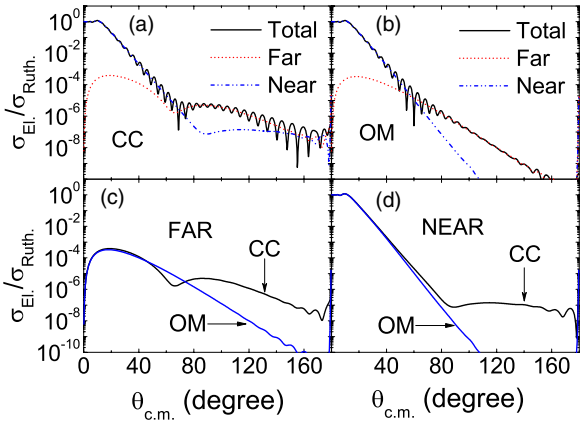

Figure 9. (a) and (b) Total, near-side and far-side elastic scattering cross sections obtained in the CC (a) and standard OM (b) approaches. (c) and (d) Comparison between the CC and OM results for the far-side (c) and near-side (d) components.

6. Near–far decomposition

As we have just shown, the sign of the deflection angle cannot be extracted from the phase-shifts without ambiguity. The use of equations (10) and (11) allows us to circumvent this problem, by decomposing the cross section into near ($\Theta > 0$) and far ($\Theta < 0$) components.

Figure 9 presents the results of the total, near-side and far-side cross sections within the CC and standard OM approaches. The comparison between the far-side components from OM and CC calculations (see figure 9(c)) suggests the presence of a nuclear rainbow bump in the CC results at $\theta \approx 85^\circ$. On the other hand, the CC near-side component also presents a bump at around 110° (see figure 9(d)). The presence of bumps in both near-side and far-side components of the CC calculations indicates the effects of the couplings on the cross sections arising from regions of small (nuclear) and large (Coulomb) angular momenta (or, classically, small and large impact parameters). On the other hand, as clearly shown in figure 9(c), the far-side (or refractive) component represents the major contribution to the total CC elastic cross sections for $\theta \geqslant 80^\circ$.

The change of the slope of the far component of the CC elastic cross section as a function of increasing angle, forming an Airy-like minimum at $\sim 65^\circ$ and a wide bump around 85°, is what we consider to be characteristic of a rainbow pattern. The experimental data, limited to $\theta \leqslant 75^\circ$, are consistent with the initial trend of this pattern: the reduction of the cross section with relation to the pure OM (with $N_I = 0.6$) result.

Returning to figure 7 bottom, it can be seen that the coupling reduces the absorption (increases the modulus of S) for $25 < \ell < 35$. These partial waves can therefore be associated with the change in cross section at large angles ($\theta > 60^\circ$) in the CC near and far components (figure 9 (c) and (d)). However, this angular momentum range is associated with scattering angles below $\theta = 60^\circ$ in all absorptive quantum results (figure 7 top). This can be interpreted as being due to the predominant reflection of these partial waves at the surface of the absorbing (complex) potential. On the other hand, those angular momenta are associated with large angles in the *classical* ($N_I = 0$) result. We suggest that, in the CC case, a small refractive component penetrates more deeply into the surface, originating the rainbow. This refractive effect is not apparent in the quantum deflection function which only evidences the predominantly reflective component. Pereira *et al* in [22] show that the strength of the imaginary part of the coupling polarization potential could be sufficient to almost cancel the imaginary potential at certain distances. This could explain how the refractive component survives, even in the absorptive CC case, to contribute to large scattering angles in the rainbow region.

7. Conclusion

We have studied the rainbow-like pattern in the elastic scattering cross sections for the ^{16}O + ^{27}Al system at $E_{\text{lab.}} = 100$ MeV. This phenomenon is associated with the change of the slope of the elastic cross section as a function of increasing angle, due to the formation of an Airy-like minimum at $\theta \approx 65^\circ$ and a wide bump around 85° in the far-side component of the scattering. This effect arises from the couplings and is not present in pure OM calculations. Although the absolute cross sections are small, these refractive effects are dominant at large scattering angles, which opens up the possibility of obtaining experimental information from deeper regions of the nucleus–nucleus potential. Currently, the experimental elastic scattering data are available up to $\theta \approx 75^\circ$, and are in agreement with the predictions. The CC cross sections are also in good agreement with the inelastic data set. Extension of the elastic scattering data to backward angles and/or to higher energy is important to thoroughly investigate this phenomenon. On the other hand, our theoretical calculations clearly indicate that the effects of couplings can be quite relevant to the elastic scattering process even at high energies.

Acknowledgments

Discussions with Professor Mahir S Hussein are gratefully acknowledged. This work was partially supported by Fundação de Amparo à Pesquisa do Estado de São Paulo (FAPESP), Fundação de Amparo à Pesquisa do Estado do Rio de Janeiro (FAPERJ), Conselho Nacional de Desenvolvimento Científico e Tecnológico (CNPq), Coordenação de Aperfeiçoamento de Pessoal de Nível Superior (CAPES) and Istituto Nazionale di Fisica Nucleare (INFN).

References

[1] Brandan M E and Satchler G R 1997 *Phys. Rep.* **285** 143
[2] Khoa D T, von Oertzen W, Bohlen H G and Ohkubo S 2007 *J. Phys. G: Nucl. Part. Phys.* **34** R111
[3] Hussein M S and McVoy K W 1984 *Prog. Part. Nucl. Phys.* **12** 103

[4] Brandan M E, Fricke S H and McVoy K W 1988 *Phys. Rev.* C **38** 673
[5] Fricke S H, Brandan M E and McVoy K W 1988 *Phys. Rev.* C **38** 682
[6] Hussein M S and Satchler G R 1994 *Nucl. Phys.* A **567** 165
[7] Fuller R C 1975 *Phys. Lett.* B **57** 217
[8] Fuller R C 1975 *Phys. Rev.* C **12** 1561
[9] Gelbke C K 1974 *Z. Phys.* **271** 399
[10] Harney H L, Braun-Munzinger P and Gelbke C K 1974 *Z. Phys.* **269** 339
[11] Cavallaro M *et al* 2011 *Nucl. Instrum. Methods* **648** 46
[12] Pereira D *et al* 2012 *Phys. Lett.* B **710** 426
[13] Chamon L C *et al* 2002 *Phys. Rev.* C **66** 014610
[14] Alvarez M A G, Chamon L C, Hussein M S, Pereira D, Gasques L R, Rossi E S Jr and Silva C P 2003 *Nucl. Phys.* A **723** 93
[15] Thompson I J 1988 *Comput. Phys. Rep.* **7** 167
[16] Pereira D, Lubian J, Oliveira J R B, Souza D P and Chamon L C 2009 *Phys. Lett.* B **670** 330
[17] Yamaya T, Satoh O, Morita S M, Kotajima K, Hasegawa K, Shinozuka T and Fujioka M 1988 *Phys. Rev.* C **37** 2585
[18] Pereira D *et al* 2012 *AIP Conf. Proc.* **1491** 353
[19] Herb J, Meerwald P, Moritz M J and Friedrich H 1999 *Phys. Rev.* A **60** 853
[20] Frahn W E 1971 *Phys. Rev. Lett.* **26** 568
[21] Bohlen H G *et al* 1985 *Z . Phys.* A **322** 241
[22] Pereira D *et al* 2013 *AIP Conf. Proc.* **1529** 274